

**EXPERIMENTAL ANALYSIS OF DIFFRACTION
EFFECTS FROM A SEGMENTED MEMS
DEFORMABLE MIRROR FOR A CLOSED LOOP
ADAPTIVE OPTICS SYSTEM: POSTPRINT**

Katia Shtyrkova, et al.

**Air Force Research Laboratory
3500 Aberdeen Ave SE
Kirtland AFB, NM 87117**

01 June 2010

Technical Paper

APPROVED FOR PUBLIC RELEASE; DISTRIBUTION IS UNLIMITED.



**AIR FORCE RESEARCH LABORATORY
Directed Energy Directorate
3550 Aberdeen Ave SE
AIR FORCE MATERIEL COMMAND
KIRTLAND AIR FORCE BASE, NM 87117-5776**

REPORT DOCUMENTATION PAGE			<i>Form Approved</i> <i>OMB No. 0704-0188</i>		
Public reporting burden for this collection of information is estimated to average 1 hour per response, including the time for reviewing instructions, searching existing data sources, gathering and maintaining the data needed, and completing and reviewing this collection of information. Send comments regarding this burden estimate or any other aspect of this collection of information, including suggestions for reducing this burden to Department of Defense, Washington Headquarters Services, Directorate for Information Operations and Reports (0704-0188), 1215 Jefferson Davis Highway, Suite 1204, Arlington, VA 22202-4302. Respondents should be aware that notwithstanding any other provision of law, no person shall be subject to any penalty for failing to comply with a collection of information if it does not display a currently valid OMB control number. PLEASE DO NOT RETURN YOUR FORM TO THE ABOVE ADDRESS.					
1. REPORT DATE (DD-MM-YYYY) 01-06-2010		2. REPORT TYPE Technical Paper		3. DATES COVERED (From - To) Oct 1, 2009- Jun 1, 2010	
4. TITLE AND SUBTITLE Experimental Analysis of Diffraction Effects from a Segmented MEMS Deformable Mirror for a Closed Loop Adaptive Optics System: Postprint			5a. CONTRACT NUMBER In House DF702204		
			5b. GRANT NUMBER		
			5c. PROGRAM ELEMENT NUMBER		
6. AUTHOR(S) Katia Shtyrova, **Loretta Arguello, *Denis Oesch, Darryl J. Sanchez, Patrick Kelly, Carylton Tewksbury-Christle, Julie Smith			5d. PROJECT NUMBER		
			5e. TASK NUMBER		
			5f. WORK UNIT NUMBER		
7. PERFORMING ORGANIZATION NAME(S) AND ADDRESS(ES) Air Force Research Laboratory *Science Applications Int **Boeing LTS 3500 Aberdeen Ave SE 6109 Airpark Rd Southeast PO Box 5670 Kirtland AFB, NM 87117 Albuquerque, NM 87106 Kirtland AFB, NM			8. PERFORMING ORGANIZATION REPORT NUMBER		
9. SPONSORING / MONITORING AGENCY NAME(S) AND ADDRESS(ES) Air Force Research Laboratory 3500 Abereen Ave Kirtland AFB, NM 87117			10. SPONSOR/MONITOR'S ACRONYM(S) AFRL/RDS		
			11. SPONSOR/MONITOR'S REPORT NUMBER(S) AFRL-RD-PS-TP-2010-1026		
12. DISTRIBUTION / AVAILABILITY STATEMENT Approved for Public Release					
13. SUPPLEMENTARY NOTES Accepted for publication in the SPIE annual conference; August 2010; San Diego, CA. 377ABW-2010-1101, July 06, 2010. "GOVERNMENT PURPOSE RIGHTS"					
14. ABSTRACT Micro-Electro-Machined Systems (MEMS) have been increasingly used as mirrors in place of conventional continuous face sheet deformable mirrors (DM) in adaptive optics (AO) systems. Here we study the diffraction effects introduced into the optical path when a segmented MEMS DM is used to correct for the wavefront aberrations. Diffraction effects are monitored through the intermediate focus plane prior to the wavefront sensor. Low pass spatial filter is used at the plane in order to investigate how the making of various diffraction orders affects the phase. Measured phase and focal image plane data for various turbulence conditions are presented and analyzed.					
15. SUBJECT TERMS Adaptive Optics, MEMS, Diffraction, Spatial Filtering, Segmented DM					
16. SECURITY CLASSIFICATION OF:			17. LIMITATION OF ABSTRACT SAR	18. NUMBER OF PAGES 18	19a. NAME OF RESPONSIBLE PERSON Patrick Kelly
a. REPORT Unclassified	b. ABSTRACT Unclassified	c. THIS PAGE Unclassified			19b. TELEPHONE NUMBER (include area code) 505-846-2094

This page is intentionally left blank.

Experimental Analysis of Diffraction Effects from a Segmented MEMS Deformable Mirror for a Closed Loop Adaptive Optics System.

Katia Shtyrkova^a, Loretta Arguello^b, Denis Oesch^c, Darryl J. Sanchez^a, Patrick Kelly^a, Carolyn Tewksbury-Christle^a, and Julie Smith^a

^aAir Force Research Laboratory, 3550 Aberdeen Ave SE, Kirtland AFB, NM;

^bBoeing-LTS, PO Box 5670, Kirtland AFB, NM;

^cScience Applications International Corp., Albuquerque, NM

ABSTRACT

Micro-Electro-Machined Systems (MEMS) have been increasingly used as mirrors in place of conventional continuous face sheet deformable mirrors (DM) in adaptive optics (AO) systems. Here we study the diffraction effects introduced into the optical path when a segmented MEMS DM is used to correct for the wavefront aberrations. Diffraction effects are monitored through the intermediate focus plane prior to the wavefront sensor. Low pass spatial filter is used at that plane in order to investigate how the masking of various diffraction orders affects the phase. Measured phase and focal image plane data for various turbulence conditions are presented and analyzed.

Keywords: adaptive optics, MEMS, diffraction, spatial filtering, segmented DM

1. INTRODUCTION

Segmented deformable mirrors provide numerous advantages over continuous face sheet deformable mirrors when used in closed loop adaptive optics systems, such as compact size, decreased cost of fabrication, and simplicity of operation. However, while conventional deformable mirrors have been used in AO systems for decades, and thus have been extensively studied and analyzed,¹ MEMS mirrors are relatively new AO technology that needs to be further investigated.²⁻⁴ A particular issue that we will investigate arises from the segmented nature of the mirror. Individual segments, along with the inter-segment spacing, create a periodic pattern that acts as a finite extent diffraction grating. The resulting multiple diffraction orders can create several potential problems for the robust performance of the AO systems, such as losing some of the light to higher order diffraction terms, and creating additional phase errors in the wavefront sensor (WFS) plane. Since the phase in the WFS pupil plane is measured and subsequently used to reconstruct the wavefront, any errors in this phase lead directly to the degradation of the Strehl ratio of the AO system. Much of the AO research is focused on predicting and reducing phase errors resulting from various sources.⁵ Any effects that are superimposed on the phase due to the segmented nature of the DM would thus inevitably result in decreased closed loop AO performance. Theoretical and experimental demonstration of the system performance changes due to segmented nature of the DM could provide insight into finding the best solution to eliminate such effects. Such theoretical work has been done previously for large astronomical telescopes with segmented primary mirrors, with virtually all the work done for the hexagonal shape segments in various configurations.^{6,7} This work is unique in that we are looking at the effects from an array of rectangular actuators, with inter-segment spacing varying due to actuator stroke during closed loop runs. In addition, the effects from atmospheric turbulence and changing the shape of the segmented DM in a closed loop AO runs couple with those of the segmentation-induced diffraction. In this paper we set the stage for the series of experiments that would attempt to investigate the spatial frequency content of the wavefront phase, both with and without atmosphere-induced aberrations, and try to use this information for removing the diffraction effects induced by the segmented nature of the MEMS DM.

In the Air Force Research Lab(AFRL)'s ASALT lab, which is a part of the Starfire Optical Range (SOR) community, the MEMS deformable mirror device was initially integrated in 2008. It was noticed that the performance of the closed loop AO runs was not as good as expected, with Strehl ratios being lower than

expected even at moderately high r_0 values with little scintillation present. This led to the investigation of possible reasons for such behavior, and one of the proposed reasons was the possibility of the segmentation-induced diffraction effects negatively affecting the phase at the WFS pupil plane. It was immediately apparent that the existing optical path for the WFS from MEMS DM was implemented without considering diffraction effects at all. Moreover, the path made intermediate focus plane prior to the pupil at the WFS inaccessible on the bench, and thus the studies of the proposed diffraction effects could not be conducted. It was proposed that a new design of the WFS optical path be modeled, and implemented, and changes be made in such a way as to minimize the segmentation induced diffraction where possible.

This new optical path design was initially modeled in a ray tracing software (Section 5), taking into consideration physical and mechanical parameters on the bench coming from MEMS DM itself (modeled as a 2D diffraction grating), intrinsic properties of the beam prior to reaching the MEMS DM, the desired quality of the pupil, and parameters of the focal plane prior to the WFS. While ray tracing software provided useful insight on the proposed diffraction effects, it could not provide for accurate intensity distributions at the focal plane, which needed physical optics rather than a ray tracing approach. Standard diffraction theory was applied to the folded and reduced newly designed optical system (Section 3) to better model and estimate the intensity distribution resulting from the MEMS DM without any atmospheric turbulence. In order to model the effects of the atmospheric turbulence at the focal plane, phase and amplitude data were taken for three different atmospheric turbulence sets for two different light paths - one that included MEMS DM in the pupil plane, and another one that completely by-passed it (Section 4). By comparing those two data sets, the segmentation-induced diffraction effects became apparent. Based on such the physical and geometrical models, along with the aforementioned data analysis, the first attempt of the new WFS path design was implemented: and a variable circular aperture field stop was introduced into the focal plane prior to the WFS in order to begin the aforementioned investigations of spatial frequency content of the atmospheric turbulence, and its coupling with the segmentation-induced diffraction effects.

2. SEGMENTED DM AND WFS SPECIFICS

The segmented deformable mirror used in this experiment was a Boston Micromachines MEMS device, with a square array of 32x32 actuators, having a pixel pitch of 300 μ m and a fill factor of 98%. Actuator throw for this device is 1.5 μ m, with the power consumption of 40W, and a total weight of less than 5kg. Only inner 30x30 actuators, masked by a circular pupil size, were actively used in closed loop AO runs.

The wavefront sensor used in conjunction with the MEMS DM was a Self-Referencing Interferometer, which measures the phase by taking four intensity profile images, phase-shifted by a known amount by using a fiber phase-shifter.⁸ The conjugate of the phase is then reconstructed on the DM mirror by re-sizing and re-scaling measured phase to fit the array of the active actuators. Figure 1 (a) shows the snap shot of the camera that

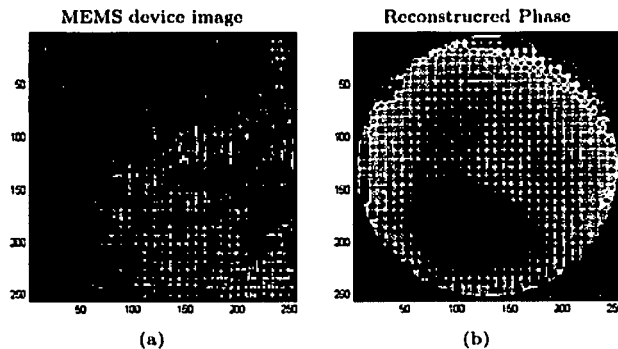


Figure 1. Image of the MEMS device after being illuminated by the system's point source.

looks at the segmented DM, without any turbulence present. The structure of the mirror is readily visible and apparent in the pupil plane. Figure 1 (b) shows a snap shot of the reconstructed phase, with the gridlines being

visibly reconstructed. Such gridlines are obviously not present in the original beam and are the artifacts of the segmented nature of MEMS DM. The important point is that the SRI WFS in ASALT lab oversamples the pupil by the factor of 8, with each sub-aperture on the MEMS DM being mapped into 8×8 pixels on the WFS camera. This effectively allows for seeing higher frequency pupil structure associated with the segmentation of the DM, which, in most astronomical telescopes, would not be visible due to having only one WFS detector for each sub-aperture. Whether or not the gridlines are visible on the WFS, they unavoidably act as a diffraction grating, creating multiple diffraction orders that make it into the final pupil plane at the wavefront sensor, unless they are either vignetted by the system or intentionally removed.

3. DIFFRACTION THEORY APPLIED TO MEMS DM, NO TURBULENCE CASE

Theoretical treatment of the diffraction produced by the MEMS device described in Section 2 is necessary prior to implementing the WFS path on the bench. With certain exceptions, deformable mirrors used for closed loop AO correction are located in collimated space, in the pupil plane. We can thus assume that, without the atmosphere, the DM is illuminated by the plane wave with uniform amplitude. The pupil is then ultimately relayed into the wavefront sensor plane, with light coming to focus in between the two pupils. The unfolded optical path leading to this intermediate focal plane can be reduced to a single lens, with the pupil located a certain distance in front of it.

The electric field distribution at the focal plane of a lens with a focal length f , for an object placed a distance d in front of the lens illuminated by a plane wave with wavelength λ can be found from Equation 1,⁹ where x and y are pupil coordinates in the starting plane. The integral in Equation 1 is the Fourier Transform of the pupil function, which, in our case, is a square array of actuators masked by a circular pupil size. The final light intensity at the focal plane is given as the square of the absolute value of the electric field (Equation 3).

$$U_f(X, Y) = A \frac{e^{i \frac{k}{2f}(1-\frac{d}{f})(x^2+y^2)}}{i\lambda f} \iint_{-\infty}^{\infty} t_A(x, y) e^{-j \frac{k}{2f}(\xi x + \eta y)} d\xi d\eta \quad (1)$$

$$U_f(X, Y) = A \frac{e^{i \frac{k}{2f}(1-\frac{d}{f})(x^2+y^2)}}{i\lambda f} F\{P(x, y)\}_{\xi=\frac{x}{\lambda f}, \eta=\frac{y}{\lambda f}} \quad (2)$$

$$I(X, Y) = \frac{A^2}{(\lambda f)^2} |F\{P(x, y)\}_{\xi=\frac{x}{\lambda f}, \eta=\frac{y}{\lambda f}}|^2 \quad (3)$$

The pupil transmission function is $P(x, y) = C(x, y) \times A(x, y)$, where $A(x, y)$ represents the array of square actuators, and $C(x, y)$ represents the circular beam, incident on the MEMS DM, located in the pupil. The actuator array can be represented by Equation 4 as a sum of shifted rect functions of width d , where d is the size dimension of the actuator, and a is the spacing between the actuators. Note that the summation goes from 1 to 16 to represent all 32×32 actuators. $C(x, y)$, defined by Equation 5, is equal to one in the pupil, and zero outside of it. The Fourier Transform of the $P(x, y)$ is thus the convolution of the two separate Fourier Transforms, as shown in Equation 6. Combining Equations 3-6, the final intensity in the pupil plane is given by Equation 7, where $Somb(r)$ is a Sombrero function, defined as $somb(r) = \frac{2J_1(\pi r)}{\pi r}$ by Gaskill,¹⁰ where $r = \sqrt{(\xi^2 + \eta^2)}$. It produces a typical Airy pattern with $D_{Airy} = 2.44\lambda \frac{f}{D_{pupil}}$, which, in our case, is $D_{Airy} = 181.71\mu m$. From Equation 7, the width of the central diffraction peak of the focal plane intensity profile is determined by the pupil diameter itself, the separation between the peaks is determined by the actuator pitch, and the amount of light in each peak depends on the ratio between parameters d and a . The amount of light in higher order peaks is inversely proportional to the fill factor of the MEMS DM. The smaller the inter-actuator gap, the less light is being lost, and the less light is being diffracted to higher orders. For the purpose of this paper we find the separation between the 0th and the 1st order maxima. The first term in the cosine summation from Equation 7 defines the maxima of the function. Maxima of the intensity peaks are taken from the \cos^2 function with $n=1$: $\cos^2(2\pi(n - \frac{1}{2})\xi(a + d)) = 1$, $(2\pi(n - \frac{1}{2})\xi(a + d)) = \pi m$; in our case $(a + d) = 300\mu m$, $\xi = \frac{x}{\lambda f}$, with $\lambda = 1.55\mu m$, and $f = 432mm$, which for the 1st order gives $X = 2.234mm$. System parameter values for the performed calculations come from the optical design outlined in Section 5.

$$A(x, y) = \sum_{m=1}^{16} \sum_{n=1}^{16} \left[\text{rect} \left(\frac{x + (n - \frac{1}{2})(a + d)}{d} \right) + \text{rect} \left(\frac{x - (n - \frac{1}{2})(a + d)}{d} \right) \right] \times \left[\text{rect} \left(\frac{y + (m - \frac{1}{2})(a + d)}{d} \right) + \text{rect} \left(\frac{y - (m - \frac{1}{2})(a + d)}{d} \right) \right] \quad (4)$$

$$C(x, y) = \text{cyl} \left(\frac{\sqrt{x^2 + y^2}}{D_{\text{Pupil}}} \right) \quad (5)$$

$$F\{P(x, y)\} = F\{A(x, y) \times C(x, y)\} = F\{A(x, y)\} * * F\{C(x, y)\} \quad (6)$$

$$I(X, Y) = \frac{A^2}{(\lambda f)^2} |F\{P(x, y)\}_{\xi=\frac{x}{\lambda f}; \eta=\frac{y}{\lambda f}}|^2 = \frac{16d^4 A^2}{(\lambda f)^2} \left(\text{Sinc}^2(d\xi, d\eta) \left[\sum_{m=1}^{16} \sum_{n=1}^{16} \cos(2\pi\xi(n - \frac{1}{2})(a + d)) \cos(2\pi\eta(m - \frac{1}{2})(a + d)) \right]^2 \right) * \frac{\pi^2 D_{\text{pupil}}^4}{16} \left(\text{somb} \left(D_{\text{pupil}} \sqrt{\xi^2 + \eta^2} \right) \right)^2 \quad (7)$$

Figure 2 shows 1D (a) and 2D (b) intensity profiles given by Equation 7. Both plots show the logarithm of the intensity. Due to the very small size of the inter-actuator gap compared with the width of the actuator, initial pupil was sampled at Nyquist frequency in order to get accurate representation of the focal plane image. In cases where the array sizes become impracticable to sample directly, Grey pixel approximation algorithm¹¹ can be used, which allows for a simple technique to model the effects of the segmentation grid without excessive calculation time and overly large arrays. Note that the powers in each successive peak in Figure 2 are not necessarily lower than in preceding peaks, since this depends on the correlation of the grid function spectrum and the sub-aperture spectrum.

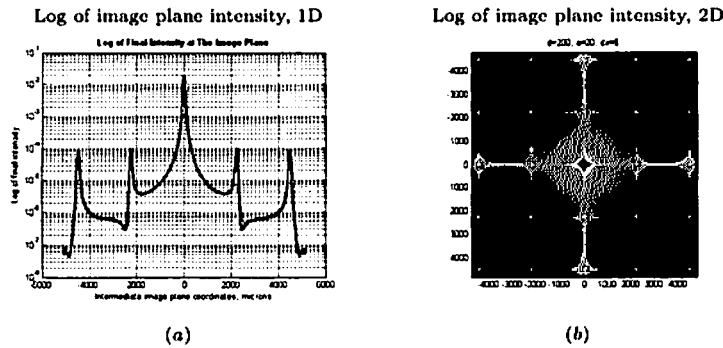


Figure 2. Logarithm of intensity at the focal plane, for no turbulence case, as modeled with the standard diffraction theory. (a) 1D profile; (b) 2D profile.

Low pass filtering the beam involves applying a mask at the focal plane that would get rid of all higher order spatial frequencies. With a circular diameter aperture stop serving as a filter, the transmission function of the filter is given by Equation 8. The resulting electric field profile, given by Equation 9 for unit magnification, is the convolution of the original electric field distribution at the MEMS DM pupil plane, with the Fourier Transform

of the filter. Figure 3 (b) shows focal plane intensity with such filter applied. Images (c) and (d) from Figure 3 show the pupil function before and after filtering.

$$T_{filter} = cyl\left(\frac{r(X,Y)}{D_{filter}}\right) \quad (8)$$

$$E(u,v) = P(u,v) * * \frac{\pi}{4} D_{filter}^2 somb(D_{filter}\rho) \quad (9)$$

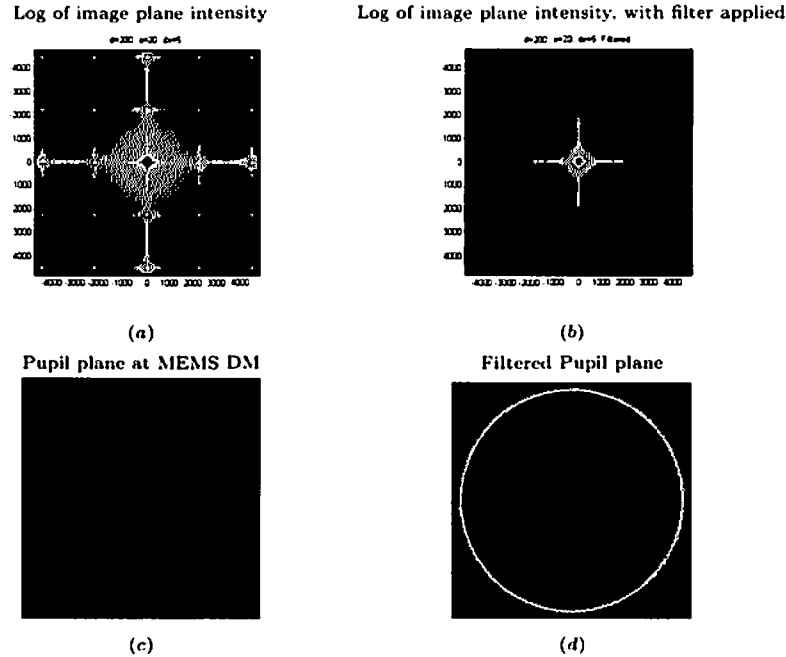


Figure 3. Top row: intensity profiles for no turbulence case for: (a) focal plane intensity, (b) focal plane intensity with low pass filter applied. Bottom row: Electric field distribution (a) pupil at MEMS DM, (b) filtered pupil.

4. MODELING DIFFRACTION EFFECTS WITH TURBULENCE PRESENT

While it is possible to analytically model the intensity distribution at the focal plane preceding the WFS with turbulence present, such distribution can also be reconstructed from SRI WFS data. Since SRI ultimately returns the phase and the amplitude at the pupil, the focal plane intensity could be reconstructed as $I(X,Y) = |F\{A(x,y)e^{i2\pi\phi(x,y)}\}|^2$, where $A(x,y)$ and $\phi(x,y)$ are amplitude and phase as calculated from SRI data. The optical path to the SRI sensor used for this data collection includes a kinematic mirror mount which allows the beam to by-pass the MEMS DM path completely, preserving the same beam size, and relaying the beam into the same pupil plane with correct magnification. The data was first taken with such mirror mount in place, followed by this mount being removed. This allowed for direct comparison of the spatial extent of the images reconstructed from SRI data with and without the MEMS DM grid present at the pupil. The no turbulence case intensity profiles are shown in Figure 4, which is effectively a PSF of the system for each of the proposed cases. Periodic dot pattern in Figure 4, right, is the direct result of the MEMS DM present in the path. This distribution is subsequently convoluted (in the final image plane) with the atmospheric disturbance profile introduced into the system by atmospheric turbulence simulator.

SRI WFS data for MEMS DM in and out of the path was taken for three atmospheric parameter sets. All three atmospheres chosen have a low Rytov parameter (under 0.1), and Greenwood frequency of $f_G=33.8$ Hz.

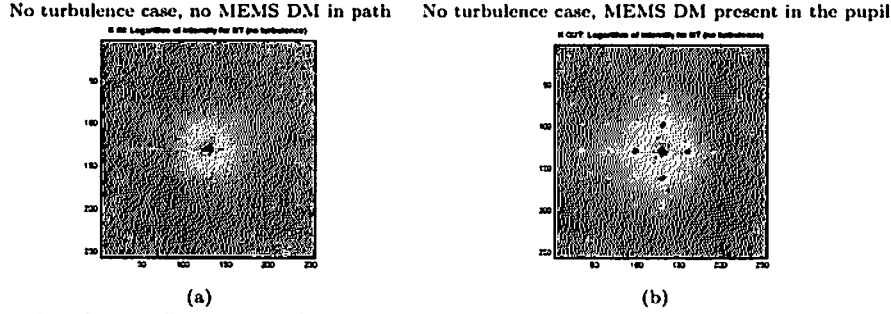


Figure 4. Intensity distribution (logarithm of) in the image plane preceding the SRI WFS., as reconstructed from the amplitude and phase data. No turbulence present. (a) no MEMS DM in the light path; (b) MEMS DM present in the pupil.

Three r_0 values (in 1.5 m space) chosen for this experiment were: 5.01 cm, 10.6 cm, 17.27cm. Figure 5 shows the intensity profiles for the three r_0 values chosen, where r_0 increases from the left to the right. Top row shows the intensity profiles for the kinematic mirror mount present in the path, and thus with no MEMS DM. Bottom row shows the intensity profiles with kinematic mirror taken out of the path, and thus having MEMS DM in the pupil of the system. It is evident that low r_0 values manifest themselves into greater intensity FWHM values, which ultimately blend in with the diffraction effects. The lower the r_0 , the harder it is to de-couple the diffraction and turbulence from the focal plane intensity data.

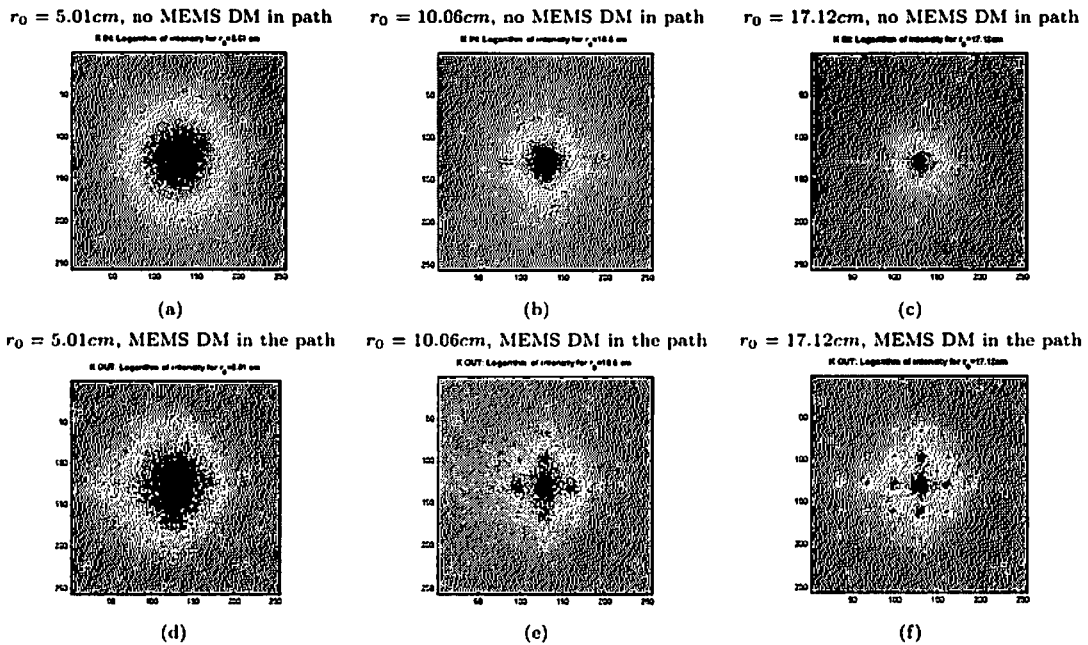


Figure 5. Intensity distribution (logarithm of), for three different r_0 values, for MEMS DM absent from the path (a, b, c), and for MEMS DM in the pupil plane (d, e, f). Reconstructed from the amplitude and phase data as taken from SRI WFS.

Figure 6 shows 1D intensity profiles, taken directly from 2D intensity data shown in Figure 5 by summing the arrays in one dimension. The data is plotted for each r_0 value separately, and it is evident how the higher order diffraction peaks bleed through the distribution due to the turbulence. In particular, for lower r_0 values, the FWHM of the intensity distribution is greater. In this case, if the spatial filter is applied in such a way

as to remove higher diffraction order peaks, some phase information will be lost as well. The wavefront sensor will never detect it, and thus will not be able to reconstruct the phase properly. This effect would be more apparent for lower r_0 values, which have wider distribution in the intensity plane. Applying the spatial filter at this intermediate image plane for higher r_0 values is still a possibility. We note that while the data shown in Figures 4 - 6 was taken from the open loop data, closing the loop will not change the results significantly. The FWHM of the intensity distribution from Figure 6 will tend to approach that of the no turbulence case. Lower r_0 values will form spots with higher FWHM, which would limit the extent of the spatial filter, and ultimately will not allow to block the unwanted diffraction effects.

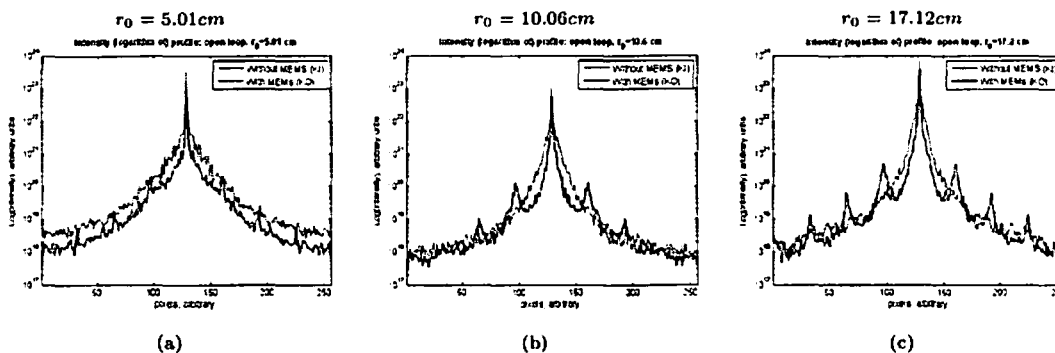


Figure 6. Intensity distribution (logarithm of), in 1D, for three different r_0 values, MEMS DM absent from the path vs MEMS DM present in the pupil. Reconstructed from the amplitude and phase data as taken from SRI WFS.

Low pass filtering of the intensity data shown in Figures 4-5 was done in software by applying a circular mask to the electric field distribution at the focal plane. The data was subsequently Fourier-Transformed back to give the electric field distribution at the pupil plane. The phase at the pupil plane was calculated as $\phi(u, v) = \text{atan} \left(\frac{\text{imag}(E(u, v))}{\text{real}(E(u, v))} \right)$. Figure 7 shows measured (a) and filtered (b) phase for no turbulence case, where the filter diameter was set to pass just the central order diffraction peak. For such no turbulence phase profiles, low pass filtering seems to work well to remove the gridline effect from the phase. Figure 8 shows measured (top row) and filtered (bottom row) phase profiles for the three atmospheric parameter sets chosen. It is evident that for lower r_0 values phase profiles exhibit smaller turbulence-induced features. When those smaller features combine with the artifacts resulting from MEMS DM being a segmented grid, it becomes harder to separate the two. Although filtering in each case completely removes the gridlines from the resulting phase, for lower r_0 values, some atmosphere-induced features are also removed.

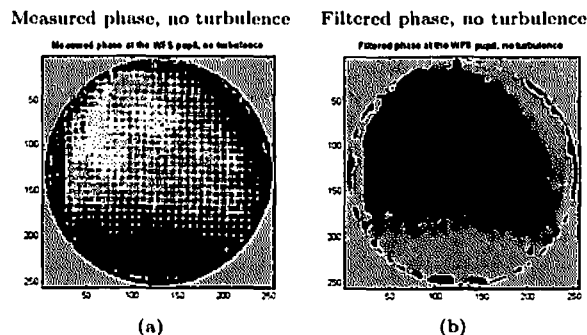


Figure 7. Phase at the pupil plane, for no turbulence present. (a) measured at the WFS pupil plane by SRI WFS, (b) filtered by the low pass filter at the focal plane.

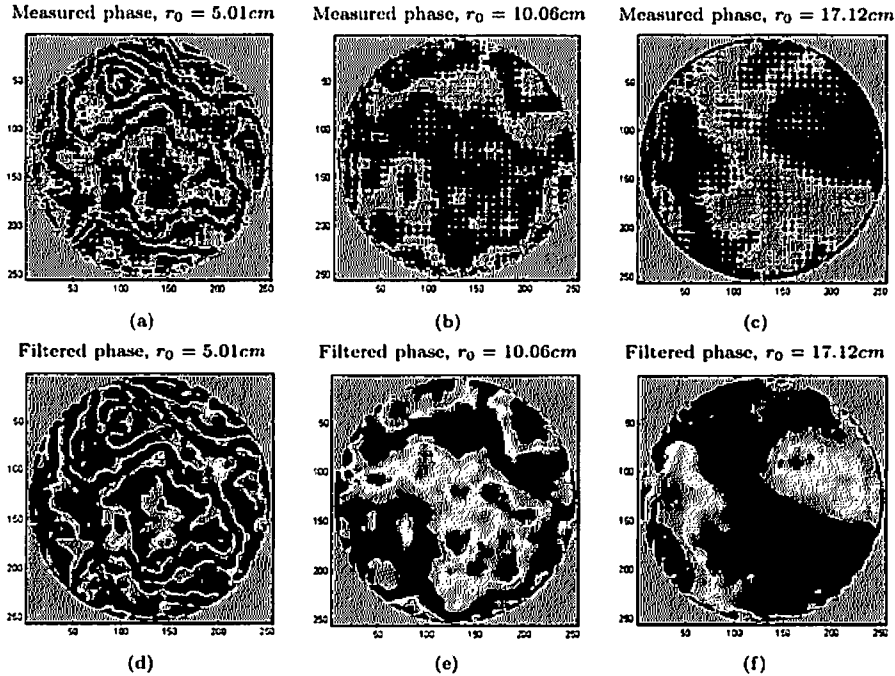


Figure 8. Phase at the pupil plane for different r_0 values. Top row - phase measured by SRI WFS at the pupil plane; bottom row - phase filtered by low pass filter at the focal plane.

5. OPTICAL DESIGN FOR SRI WFS PATH

Physical optics models from Sections 3-4, combined with the ray tracing models, were used for the final design of the new SRI WFS that would allow to investigate and correct for the diffraction effects resulting from the segmentation of the MEMS DM.

5.1 2D Grating Modeling of the MEMS DM in ray-tracing software

Prior to considering the pupil relay WFS path optical design, it is critical to be able to model MEMS DM in the ray tracing software program as a proper 2D diffraction grating reflecting the light into multiple diffraction orders. This will determine whether or not the diffracted light gets vignetted as it propagates through the optical elements, will set the desired spot separation at the focal plane, and will place constraints on the focal lengths of all powered optics used. An intuitive way to model the diffraction off the MEMS DM in the ray tracing program is by assuming that this segmented device is a 2D diffraction grating. With this assumption, two different approaches were used to model MEMS DM as a grating in Zemax software. First, a 2D grating was directly modeled as a combination of two 1D diffraction gratings, located in conjugate planes and rotated by 90 degrees with respect to each other. Second, diffracted field angles were manually calculated and propagated through the system along with the zero field. The two models were found to give essentially the same result.¹²

The first method of modeling MEMS DM in Zemax was implemented by combining two 1D gratings. Due to the fact that ZEMAX allows to easily use 1D physical optics gratings components, two gratings with 90 degree angle between them were used in two conjugate pupil planes. A one-to-one pupil relay system of two lenses was inserted prior to original MEMS location, with x-grating in the first pupil plane, and y-grating in the relayed pupil plane. The lines per micron parameter for each grating was set to 0.0033, which corresponds to 300 μm pitch between the segments of the MEMS device. The diffraction order of the original gratings was set to zero. Multiple diffraction orders were modeled in Multi-Configuration editor in ZEMAX, with each configuration having a designated diffraction order for each of the two gratings. Diffraction orders from -2 to 2 were investigated, corresponding to a total of 25 combinations when putting together x- and y- fields (25 configurations).

The second method of modeling MEMS DM in a ray tracing software was to first manually calculate the diffracted angles by using a standard grating equation (Equation 10), with $m=[-2:2]$, for both x- and y- directions. Incident angle illuminating the MEMS device is $\sim 6^\circ$, with $\lambda = 1550\text{nm}$ and $d = 300\mu\text{m}$. Table 1 shows the calculated diffraction angles, along with the field angles, which are the deviations of the higher orders from the 0th order beam. In order to model a 2D grating by using those angles, they need to be combined for x- and y- fields, producing a total of 25 field angles, which were modeled in Multi-Configuration editor due to the fact that the limit of the number of fields in any one configuration in Zemax is 12.

$$d(\sin(\theta_m) + \sin(\theta_i)) = m\lambda \tag{10}$$

Diffraction order	-2	-1	0	1	2
Diffracted angle, in degrees	5.405	5.702	6.000	6.298	6.596
Deviation from 0 th order, in degrees	-0.595	-0.298	0	0.298	0.595

Table 1. Diffracted angles and deviations from 0th order for MEMS DM, in one dimension

The results from both methods of diffraction modeling were shown to be almost identical,¹² allowing for using the methods interchangeably. Due to the fact that the field angles method did not insert extra optical elements into the lens editor, field angles model was used for all the subsequent data shown.

5.2 MEMS SRI Optical Path

Physical optics models from Sections 3 and 4, along with the geometrical optics models of the MEMS DM introduced earlier in the section, were used as a starting point for the WFS optical path design. Since both the segmented DM and the WFS camera plane must be in the pupil, the optical layout relaying the DM into the WFS must account for proper magnification, orientation and path length. In addition, for the proposed experiments the intermediate focus plane should be easily accessible and the spot separation should be sufficient enough to be able to resolve them with the camera and to mask them out. From the analysis in Section 3, the ratio between the full width of a central peak at the focal plane to the separation between the peaks will be fixed, and will depend only on intrinsic system parameters such as the beam size on the MEMS DM, the spacing between the actuators, and the width of each actuator. The 2D folded layout of the MEMS SRI WFS path, shown in Figure 9 (a) gets its shape from getting around multiple other optical and mechanical components on the bench (not shown). The final design, in addition to relay and beam directing optics, also includes an iris at the intermediate focus plane, a beam splitter that separates MEMS SRI path from the main beam path, and another beam splitter for SRI reference beam to be injected. 3D shaded model, shown in Figure 9 (b) gives a three dimensional layout of the path.

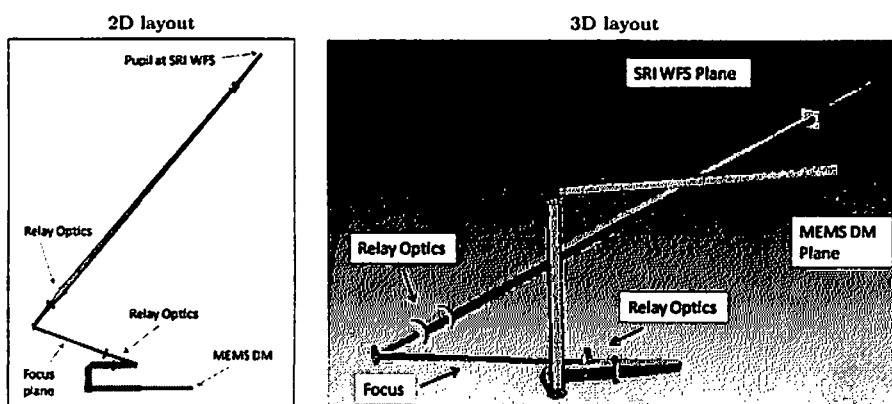


Figure 9. Layouts for MEMS SRI path. (a) 2D layout, viewed from the top; (b) 3D shaded model.

Intermediate focus plane between the two sets of relay optics shows the far field diffraction pattern, which in Zemax geometrical model shows up as distinct spots, each one corresponding to a specific diffraction order.

optics (as well as that of the second one) is significantly longer, providing for greater spot separation in the intermediate focal plane, which allows to easily mask off desired diffraction orders with conventional field stops; intermediate focal plane is far away from any optical elements and can be easily imaged by a separate camera; the design places the WFS camera away from optical components, which removes the air flow from the camera's cooling fan away from the light path. The number one advantage is that the peak-to-peak separation of the 0th and the 1st order beams is about 2.24mm, which can be easily resolved by the camera and masked off by various means.

6. INITIAL RESULTS

The optical relay system proposed in Section 5 was implemented on the ASALT Lab's optical bench, as a part of an active AO wavetrain. The iris, with diameter varying from 0.5mm to 12mm, was placed at the intermediate image plane, and the intensity at that plane was monitored by Sensors Unlimited InGaAs camera. Figure 12, (a), shows the far field intensity profile that was obtained with a 1550 nm point source as a light source, with the beam diameter at the MEMS DM being 9.00 mm. No atmospheric turbulence was used, and the flat map was applied to the DM, making the image at the focal plane close to PSF of this optical path. The foreshortening in the x- dimension is due to the fact that the camera was viewing the plane at an oblique angle. The spot separation data is in a very good agreement with the Zemax model: for the separation of the 1st order spots, Zemax model gave 2.24mm., while the same separation from the experiment was found to be 2.1744mm. Similarly the intensity distribution agreed with Matlab model: the spot separation from the model was found to be 2.234mm, while data shows it to be 2.1744mm, where the deviations between real and modeled data most likely came from the focus position error. Figure 13 (right) shows the logarithm of the final image plane intensity as modeled (see Section 3), and Figure 13 (left) shows the logarithm of the normalized sum in one direction calculated from Figure 12 data. The central peak in Figure 13, left, is a lot smaller than what is should have been, due to the central opening of the iris during the experiment.

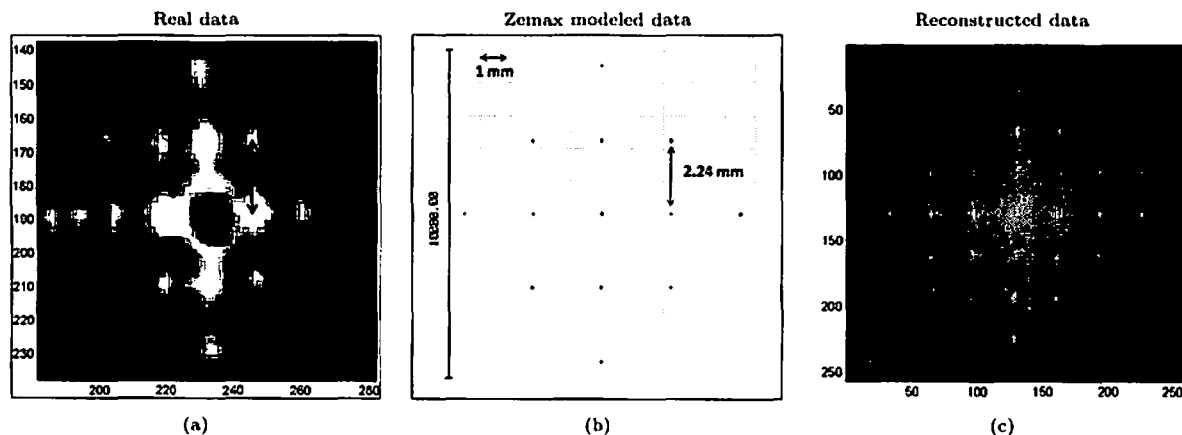


Figure 12. Far field diffraction profile, after reflecting off the segmented DM with the flat map on. (a) Real data taken by InGaAs camera, (b) Zemax modeled data, (c) Reconstructed data.

Open loop focal plane intensity profiles for three turbulence conditions described in Section 4 are shown in Figure 14. These profiles were taking by physically inserting an imaging surface into the optical path. Note that for lower r_0 values, the data is in exact agreement with the reconstructed data shown in Section 4. Moreover, separate peaks are easily resolved with the available camera and could be masked out as shown in Figure 12 (a). The turbulence intensity profiles confirm the fact that diffraction effects couple with the atmospheric turbulence, and this effect is more apparent for low r_0 values. For each turbulence case, the iris at the focal plane was stopped down to 2.2 mm in diameter, to remove the effects of the diffraction grid. Corresponding phase profiles, measured by SRI WFS, are shown in Figure 15, where the top row shows SRI-measured phase with the iris fully open(unfiltered beam), and the bottom row shows the phase with the iris stopped down. r_0 increases from the

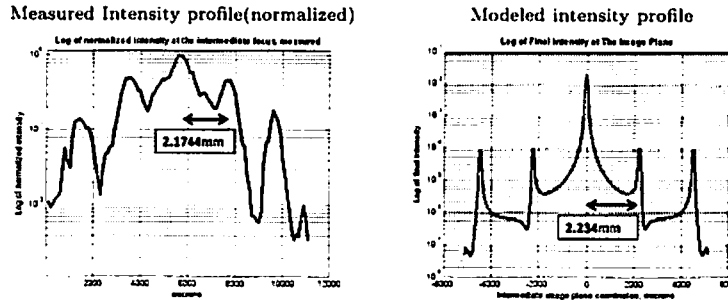


Figure 13. Intensity profiles at the image plane, measured intensity vs modeled data

left to the right. The gridline pattern resulting from MEMS DM segmentation is visibly present in the unfiltered beam at all turbulence conditions; and the pattern is completely eliminated in all cases where the iris has been stopped. However, by using the field stop of the diameter of 2.2mm in all the profiles from Figure 14, much of the turbulence information was also removed from the beam at lower r_0 values. This suggests either a different Fourier filter that would selectively suppress specific frequency components, or a dynamic low pass filter concept.

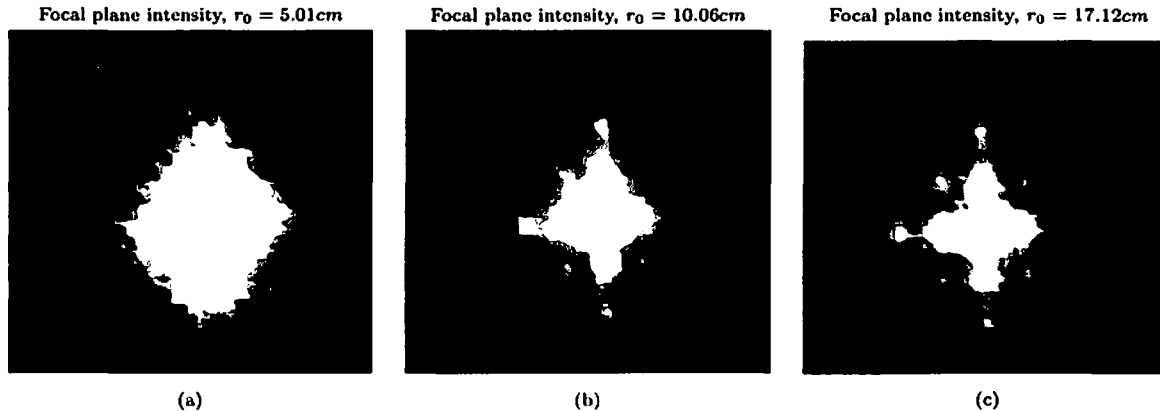


Figure 14. Far field diffraction profile, after reflecting off the segmented DM with the flat map on. (a) Real data taken by InGaAs camera, (b) Zemax modeled data, (c) Reconstructed data.

The problem of undesired elimination of some of the atmospheric turbulence features by low-pass filtering the beam in order to eliminate the errors caused by MEMS DM segments can be partially solved by having a dynamic low pass filter. The filter should be applied at the focal plane *after* the loop has been already closed. In this case, the intensity profile would change from a wider distribution of the open loop to a narrower distribution ultimately approaching the ideal vacuum case. This would allow the AO system to effectively separate the diffraction and turbulence effects by itself. Applying the filter to the closed loop profile would eliminate the diffraction effects alone, without affecting the turbulence much. The concept is illustrated in Figure 16. It is important to note that while having a dynamic low pass filter would help to reduce diffraction effects, this is not the ideal solution. In particular, for severe atmospheric turbulence conditions, the AO system does not close the loop perfectly, and the focal plane light distribution might never approach that of the vacuum case. In such a case, turbulence and diffraction effects at the focal plane would never become separated sufficiently enough to be successfully low pass filtered without negatively impacting the robustness of the AO system.

7. CONCLUSION

We demonstrated that diffraction effects from segmented nature of the MEMS DM show up clearly at the intermediate focal plane prior to the WFS as higher spatial frequency terms distributed in a characteristic

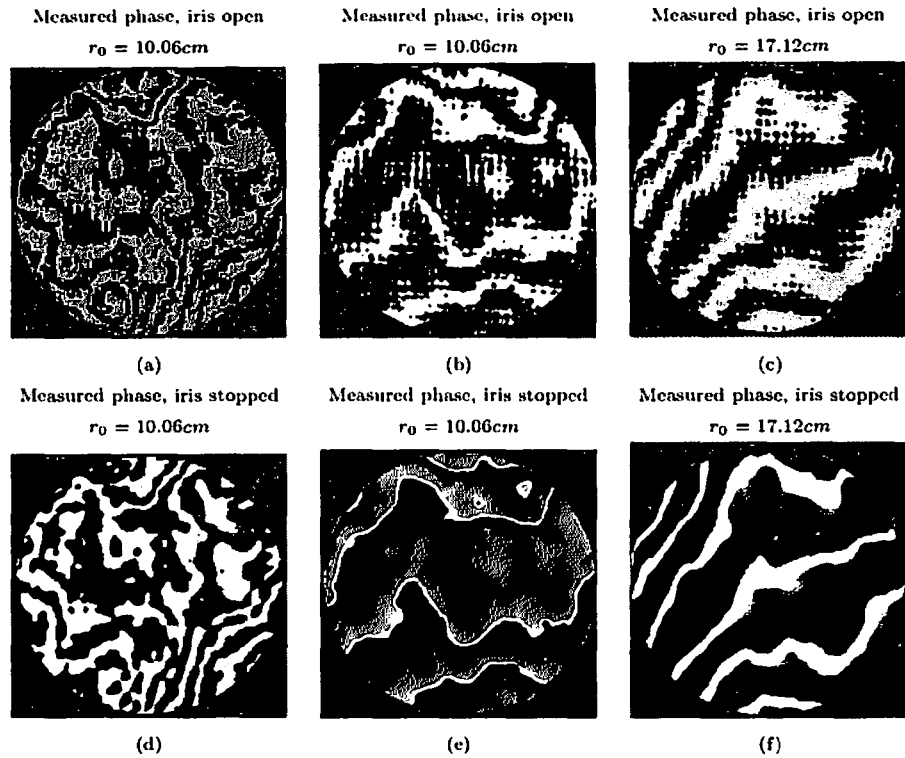


Figure 15. Phase as measured with the new SRI WFS. Top row - iris at the focal plane fully open, bottom row - iris at the focal plane stopped to remove the higher order diffraction effects.



Figure 16. Dynamic spatial filter concept illustration.

symmetrical pattern. While it is easy to mask off higher diffraction orders for no turbulence case, we have shown that for various atmospheric turbulence conditions the effects of the turbulence couple with the segmentation-induced diffraction effects, and it becomes difficult to de-couple the two. In particular, at lower r_0 values the intensity distribution at the focal plane becomes sufficiently wide as to hide the effects of the segmentation induced pattern altogether. Removing higher order diffraction terms by low-pass filtering the beam at the focal plane prior to the WFS noticeably changes measured phase. The grid effect visible in the phase without filtering the beam completely disappears with the proper filter diameter. However, at lower r_0 values, some of the atmospheric turbulence induced phase features are also removed by the low pass filter, making closed loop AO performance unstable. A better approach to removing the segmentation-induced effects from the phase would be to dynamically apply the filter, with stopping the field down after the loop has already been closed. In addition, a different Fourier filter could be used to selectively suppress just the spatial frequencies corresponding to the segmentation-induced effects.

The new SRI WFS optical path provided the insight into both the physical nature of the problem and the

future optical design modifications needed in order to have a better WFS that would both provide an excellent pupil quality and remove the segmentation-induced diffraction effects. Further experiments that investigate the dependence of the strength of the atmospheric turbulence on its spatial frequency content need to be done in order to come up with a better approach to get rid of the diffraction effects alone, taking care of not removing the essential turbulence-induced phase information from the beam. Closed loop AO runs with various turbulence conditions need to be compared for each of the methods of diffraction elimination used. In addition, while ASALT lab uses the monochromatic light, astronomical telescopes usually perform imaging in certain wavelength bands. This needs to be addressed, modeled, and compensated for in a better WFS design in conjunction with the segmented DM.

ACKNOWLEDGMENTS

We would like to express our gratitude to the Air Force Office of Scientific Research for their support in funding this research. Author would like to extend a special thank you to Michael B. Flanagan for useful discussions on Fourier filtering, and Denis W. Oesch for numerous ideas and help with this research.

REFERENCES

1. J. W. Hardy, *Adaptive Optics for Astronomical Telescopes*, Oxford University Press Inc., New York, NY, USA, 1 ed., 1998.
2. J. C. Smith, D. J. Sanchez, D. W. Oesch, P. R. Kelly, C. M. Tewksbury-Christle, and K. P. Vitayaudom, "Initial Results from Implementing and Testing a MEMS Adaptive Optics System," in *2009 SPIE Annual Conference*, R. Carerras, T. Rhoadharmer, and D. Dayton, eds., SPIE, 2009.
3. B. P. Wallace, P. J. Hampton, C. H. Bradley, and R. Conan, "Evaluation of a MEMS deformable mirror for an adaptive optics test bench," *Optics Express* 14(22), pp. 10132–10138, 2006.
4. J. C. Smith, D. J. Sanchez, D. W. Oesch, C. M. Tewksbury-Christle, Charles C. Beckner Jr., K. P. Vitayaudom, P. R. Kelly, and N. E. Glauvitz, "Direct Experimental Comparison between a MEMS Segmented Deformable Mirror and a Xinetics Deformable Mirror," in *2009 DEPS Annual Conference*, D. Herrick, ed., Directed Energy Professional Society, 2009. Published in briefing format only.
5. R. Q. Fugate, "OSA optics handout volume iii," 2000.
6. W. Yan, Y. Ji-xang, W. Bi-ru, and X. Man-jun, "Diffraction effects on image quality of segmented mirror with quasi annulus sector," in *Proceedings of SPIE, Vol. 7281*, W. Jiang, R. Geyl, and M. K. Cho, eds., SPIE, 2009.
7. N. Yaitskova, K. Dohlen, and P. Dierickx, "Diffraction in OWL: Effects of segmentation and segments edge misfigure," in *Proceedings of SPIE, Vol. 4840*, R. P. Angel and R. Gilmozzi, eds., SPIE, 2003.
8. T. A. Rhoadarmer and L. M. Klein, "Design of a spatially phase shifted self-referencing interferometer wave front sensor," in *Advanced Wavefront Control: Methods, Devices, and Applications IV*, M. K. Giles, J. D. Gonglewshi, and R. A. Carerras, eds., SPIE, 2006.
9. J. W. Goodman, *Introduction to Fourier Optics*, Roberts & Company, Englewood, CO, USA, 3 ed., 2005.
10. J. D. Gaskill, *Linear Systems, Fourier Transforms, and Optics*, John Wiley & Sons, New York, USA, 1 ed., 1978.
11. M. Troy and G. Chanan, "Diffraction effects from giant segmented mirror telescopes," in *Proceedings of SPIE, Vol. 4840*, R. P. Angel and R. Gilmozzi, eds., SPIE, 2003.
12. K. Shtyrkova, "MEMS Path Design Diffraction Modeling," (SOR Internal) ASALT TR 2009-22, ASALT Lab, 2009.
13. L. A. Poyneer and B. A. Macintosh, "Spatially filtered wave-front sensor for high-order adaptive optics," *JOSA* 21(5), pp. 810–818, 2004.

DISTRIBUTION LIST

DTIC/OCP 8725 John J. Kingman Rd, Suite 0944 Ft Belvoir, VA 22060-6218	1 cy
AFRL/RVIL Kirtland AFB, NM 87117-5776	2 cy
Patrick Kelly Official Record Copy AFRL/RDSAE	1 cy